



Contents lists available at ScienceDirect

Arabian Journal of Chemistry

journal homepage: [www.sciencedirect.com](http://www.sciencedirect.com)

Original article

# Waste rice noodle-based CQDs/ZnO composite nanorod array on steel wire mesh: Preparation and photocatalytic capability

Ruijie Che <sup>a,b</sup>, Biyang Tu <sup>b</sup>, Yining Zhu <sup>b</sup>, Jiahe Miao <sup>b</sup>, Xinyan Jin <sup>a</sup>, Shuoping Chen <sup>a,\*</sup><sup>a</sup> College of Materials Science and Engineering, Guilin University of Technology, Guilin, Guangxi 541004, China<sup>b</sup> School of Environment, Nanjing Normal University, Nanjing, Jiangsu 210023, China

## ARTICLE INFO

## Article history:

Received 16 May 2023

Accepted 31 August 2023

Available online 09 September 2023

## Keywords:

Waste rice noodle  
CQDs/ZnO composite  
Array  
Steel wire mesh  
Photocatalytic

## ABSTRACT

In order to develop cost-effective photocatalytic devices, a nanorod array-structured carbon quantum dot/zinc oxide (CQDs/ZnO) composite was synthesized on a steel wire mesh substrate using waste rice noodle (WRN) as the raw material. The incorporation of CQDs derived from WRN played a crucial role in controlling the morphology of the ZnO-based array. By optimizing the loading of CQDs, the CQDs/ZnO composite achieved a regular hexagonal prism nanorod array distribution and exhibited highly efficient photocatalytic degradation of various organic pollutants. For instance, in the case of methylene blue, the CQDs/ZnO composite demonstrated a remarkable degradation rate of 99.4% within 90 min, with a high degradation rate constant of  $0.033 \text{ min}^{-1}$ . Moreover, the composite material could be recycled and reused for five photocatalytic cycles without a significant decrease in its degradation performance, surpassing the performance of the pure ZnO array. Furthermore, the resulting CQDs/ZnO composite array exhibited effective photocatalytic degradation for other organic dyes such as malachite green, methyl violet, basic fuchsin, and rhodamine B. Additionally, this composite material was successfully applied to real water purification, achieving a high mineralization efficiency of 48% and a low leaching rate of Zn of 1.2% in a river water sample after a 90-minute photocatalytic process. The introduction of CQDs derived from WRN into the ZnO array led to efficient electron-hole pair separation, enabling more photogenerated electrons to reduce  $\text{O}_2$  and more photogenerated holes to oxidize  $\text{H}_2\text{O}$ . This resulted in enhanced radical generation and improved photocatalytic degradation of organic pollutants, showcasing the superior performance of the CQDs/ZnO composite array.

© 2023 The Author(s). Published by Elsevier B.V. on behalf of King Saud University. This is an open access article under the CC BY-NC-ND license (<http://creativecommons.org/licenses/by-nc-nd/4.0/>).

## 1. Introduction

The global environment is currently facing immense pressure, with water pollution being one of the main sources of environmental problems (Huang et al., 2022; Sarkar et al., 2017). Commonly used methods for wastewater treatment include adsorption, coagulation, precipitation, oxidation, and reduction, but these traditional approaches are prone to causing secondary pollution to water bodies and the environment (Chiu et al., 2019; Modrogan et al., 2021, 2020). Photocatalytic degradation of pollutants in

wastewater presents a more promising alternative. Over the past 50 years, semiconductor photocatalysis has been extensively employed in water treatment (Zhou et al., 2023), encompassing the degradation of various pollutants, hydrogen production, carbon dioxide reduction, and nitrogen fixation (Chang et al., 2022; Xue et al., 2022). The key to successful photocatalysis lies in the design of efficient and cost-effective photocatalysts (Gangu et al., 2019; Huszla et al., 2022). Currently, materials like  $\text{TiO}_2$ , CuO, ZnO, and  $\text{V}_2\text{O}_5$  are widely used as catalysts for photocatalytic reactions due to their strong and effective ability to combat chemical and biological pollution in water (Modrogan et al., 2021). The photocatalytic activity is largely influenced by catalyst properties, such as morphology, composition, specific surface area, and band gap width (Nicolaeescu et al., 2021). Among the various types of catalysts, zinc oxide (ZnO) has attracted significant attention for its properties of high efficiency, nontoxicity, low cost, ease of preparation and proper conduction band (CB) potential (Jiang et al., 2022b; Abdollahi et al., 2021; Gao et al., 2021; Senasu et al., 2021). ZnO is extensively used as a new type of material in various fields such

\* Corresponding author.

E-mail address: [chenshuoping\\_777@163.com](mailto:chenshuoping_777@163.com) (S. Chen).

Peer review under responsibility of King Saud University.



Production and hosting by Elsevier

as electronics, textiles, rubber, photocatalysis, and pharmaceuticals (Purcar et al., 2017). However, ZnO has a large band gap ( $E_g = 3.37$  eV), resulting in a narrow range of light absorption wavelengths, mainly concentrated in the UV band. This limitation greatly hampers its utilization of solar energy and photocatalytic efficiency (Samadi et al., 2016; Shen et al., 2022). Moreover, pristine ZnO suffers from the recombination of photogenerated electron-hole pairs (Wang et al., 2020). Numerous strategies have been explored to address these drawbacks, such as doping, constructing heterojunctions, and incorporating coupled carbon materials (Abd-Elrahim and Chun, 2021; Jiang et al., 2021; Pan et al., 2020; Zelekew et al., 2021; Zhang et al., 2023a).

The carbon quantum dots (CQDs) have attracted widespread attention in the field of photocatalytic material design due to their high water dispersibility, high stability, and low toxicity (Arumugham et al., 2020; Zhao et al., 2022). The high responsiveness to sunlight (Tang et al., 2019), ability to enhance the adsorption performance (Chen et al., 2022; Yu et al., 2022), and high resistance to photogenerated electron-hole pair recombination make CQDs a suitable candidate for improving photocatalytic efficiency (Behnood and Sodeifian, 2020; Que et al., 2017; Zhang et al., 2023b). Recently, new developments have occurred in the application of CQDs in photocatalytic materials. Behnood et al. synthesized nitrogen-doped carbon quantum dot composite nickel-doped zinc oxide (Ni-ZnO/N-CQDs) composites using a hydrothermal method. The presence of Ni and N-CQDs could promote the separation of electron-hole pairs under visible light, and 87% of methylene blue (MB) can be effectively degraded within 120 min (Behnood and Sodeifian, 2020). Mandal et al. prepared nonmetallic nitrogen-doped carbon quantum dots (N-CQDs) hybridized with zinc oxide nanorods (NRs). The degradation performance of rhodamine B on ZnO/NCQD reached approximately 90% within 9 min under ultraviolet irradiation (Mandal et al., 2021). To date, most CQDs in CQDs/ZnO composite materials reported by other researchers originate from relatively high-cost synthetic raw materials, such as glucose, sucrose, fructose, ascorbic acids, sodium citrate, and graphite rods (Han et al., 2021; Murali et al., 2021; Tan et al., 2021; Wu et al., 2019; Xu et al., 2019). Unfortunately, these raw materials are not conducive to industrial applications, especially in economically underdeveloped areas.

On the other hand, more than 1.3 billion tons of cooking waste are generated worldwide each year (Rojas et al., 2022). Because of the high levels of water and organic matter in cooking waste, its inadequate disposal can easily have several harmful effects on the environment (Li et al., 2023), including surface and ground water contamination, virus transmission, and pollutant gas emissions (Barik and Paul, 2017; Chu et al., 2019). Current commercial treatments for cooking waste mainly involve methods like anaerobic digestion (Yan et al., 2021), aerobic composting (Xie et al., 2023), landfill (Shehzad et al., 2015), incineration (Xiao et al., 2018), and forage making (Mo et al., 2020). While these strategies allow for large-scale industrialization of cooking waste treatment, they come with significant drawbacks, including extensive land use, high equipment investment, low product profit margin, and the potential for secondary pollution such as greenhouse gas emissions and waste leachates (Touze-Foltz et al., 2021). In order to address these issues, our previous investigation proposed a novel approach to utilize cooking waste, specifically waste rice noodle (WRN), with starch as the main component. This approach involved first hydrothermal carbonizing the WRN to create a solution of carbon quantum dots (CQDs), which was then combined with specific inorganic nano powders like  $\text{TiO}_2$  or ZnO to produce CQDs/ $\text{TiO}_2$  or CQDs/ZnO photocatalytic composites for water pollution control (Jin et al., 2022b; Jin et al., 2022a). For instance, the CQDs/ZnO composite based on WRN exhibited a highly efficient photocatalytic degradation effect on methylene blue, showing a

good degradation rate of 99.58% within 40 min and a high degradation rate constant of  $0.2630 \text{ min}^{-1}$ , and could be recycled and reused for ten photocatalytic cycles without an appreciable decrease in the degradation effect, which was much better than that of commercial ZnO (Jin et al., 2022b). However, as a powdered photocatalyst each recycling step of this CQDs/ZnO composite based on WRN requires careful centrifugation, washing, and drying. This process posed significant challenges when applied to large-scale wastewater treatment in practical settings. In addition, it is challenging to assemble these powdered catalysts into photocatalytic reaction devices that can be used for an extended period.

In order to meet the demands of large-scale industrial water purification, it is essential to address the challenges associated with the difficult recovery and assemble of powdered catalysts (Jiang et al., 2022a; Marugán et al., 2007; Zhang et al., 2020). One effective solution is to prepare a photocatalytic device in which the photocatalytic component could be loaded onto a low-cost and stable substrate (Misra et al., 2022; Sugita et al., 2020). Zhou et al. (Zhou et al., 2020) prepared a three-dimensional artificial nanoforest by hydrothermally loading n-type polar microporous modulated wide bandgap ZnO nanodiscs on a copper grid, showing good photocatalytic reduction activity and recyclability for aqueous hexavalent chrome [Cr(VI)]. Misra et al. (Misra et al., 2022) designed a photocatalytic device utilizing zinc oxide composite gypsum loaded with sodium alginate (ZnO/G@alginate) to achieve disinfection of *Salmonella enterica* serovars under visible light. However, due to the widespread use of expensive synthetic reagents in the preparation process of these photocatalytic devices, their high production costs may hinder practical commercialization.

Anticipating the incorporation of waste-based raw materials and the selection of appropriate low-cost substrates, it becomes feasible to design and synthesize a photocatalytic device that is not only cost-effective but also highly efficient, easy to recycle, long-lasting, and environmentally friendly. Building upon previous research, our primary objective is to develop a novel photocatalytic device comprising a CQDs/ZnO composite based on WRN, which offers advantages of lower production costs, convenient assembly, and practical application. Through the utilization of low-cost steel wire mesh as a substrate, we successfully created a budget-friendly photocatalytic device featuring a CQDs/ZnO composite nanorod array, utilizing WRN as the raw material. This resulted in the CQDs/ZnO composite array demonstrating outstanding photocatalytic degradation efficiency for various organic pollutants, thereby serving as a valuable reference for the design of efficient photocatalytic reactors. Our research delves into the morphology, structure, photocatalytic performance, and photocatalytic mechanism of the array, with a comprehensive analysis of the effects of CQDs combination on the material's morphologies and properties.

## 2. Experiment section

### 2.1. Materials

Waste rice noodles (WRN, primary organic constituents: starch 21.65 g/100 g; fat 0.4 g/100 g; protein 1.91 g/100 g) were obtained and retrieved from a Guilin-based university canteen. Stainless steel wire mesh (material: 304 stainless steel; size: 400 mesh; density:  $7.93 \text{ g/cm}^3$ ), zinc acetate dihydrate (98% purity), ammonia (28 wt% in water solution), methylene blue (98.5% purity), malachite green (98% purity), methyl violet (98% purity), basic fuchsin (98% purity), rhodamine B (98% purity), and dimethyl pyridine N-oxide (DMPO, 99% purity) were acquired from Maclean's Reagent (Shanghai, China), and all reagents were used without additional refinement.

## 2.2. Synthesis

The schematic illustration of the synthesis and device integration of the WRN-based CQDs/ZnO composite nanorod array on the steel wire mesh is shown in Fig. 1. At first, the stainless steel wire mesh was subjected to a cleaning process using acetone and anhydrous ethanol with ultrasonic treatment for 30 min, which was repeated for three times. Subsequently, the steel wire mesh was dried in a vacuum drying oven at 60 °C. Next, zinc acetate was dissolved in anhydrous ethanol to form a 0.005 mol/L ethanolic solution of Zn<sup>2+</sup> ions. The cleaned steel wire mesh was immersed in the 0.005 mol/L Zn<sup>2+</sup> ethanolic solution for approximately 10 s. and then was removed and quickly dried in a 60 °C oven for 1 h, which was repeated for four times. The stainless steel wire mesh then underwent calcination at 350 °C for 20 min using a muffle furnace.

Simultaneously, following our previously established method (Jin et al., 2022a), CQDs solution was prepared via hydrothermal treatment of the WRN. Specifically, 150 g of WRN was milled and thoroughly mixed with 300 g of deionized water. The mixture was placed in a 500 mL hydrothermal reactor (Yitron Instrument, Xian, China) lined with PTFE and heated at 200 °C for 10 h. The upper layer of the reaction product, the CQDs solution, was obtained by filtration.

Then, zinc acetate was dissolved in water to form a 0.2 mol/L aqueous solution of Zn<sup>2+</sup> ions. The resulting Zn<sup>2+</sup> solution (0.2 mol/L), ammonia, and CQDs solution were mixed in a 500 mL PTFE-lined hydrothermal reactor (Yitron Instrument, Xian, China) at a volume ratio of 3: 1 ~ 5. Subsequently, the stainless steel wire mesh that had undergone the previously mentioned treatment was placed vertically into the hydrothermal reactor and heated at 95 °C for 12 h. The resulting sample was rinsed three times with deionized water and anhydrous ethanol, followed by drying at 60 °C for 6 h. This process resulted in the final stainless steel wire mesh with the surface-loaded CQDs/ZnO composite nanorod array. The synthetic formulation and EDS elemental analysis of the CQDs/ZnO composite nanorod arrays on the steel wire mesh are presented in Table 1.

## 2.3. General characterization

The scanning electron microscope (SEM) images and energy-dispersive X-ray (EDX) elemental analysis were obtained by using an S-4800 field emission scanning electron microscope (Hitachi, Chiyoda, Tokyo, Japan) with an accelerating voltage of 20 kV. The morphology the CQDs/ZnO composite were characterized using a JEM-2100F field emission transmission electron microscope (TEM, JEOL, Akishima, Tokyo, Japan) with an accelerating voltage of 200 kV. The X-ray photoelectron spectroscopy (XPS) of the CQDs/ZnO composite and ZnO was carried out using an ESCALAB 250Xi X-ray photoelectron spectrometer (Thermo Fisher, Waltham, MA, USA) with an Al K $\alpha$  X-ray as the stimulating source.

The UV–VIS absorption spectra of the CQDs/ZnO composite and ZnO array were measured using a UV3100 UV–VIS–NIR spectrophotometer (Shimadzu, Chiyoda, Tokyo, Japan) in diffuse reflection mode, with BaSO<sub>4</sub> as the reference material. The photoluminescence spectra of the CQDs/ZnO composite and ZnO array were examined using a Cary Eclipse fluorescence spectrophotometer (Varian, Palo Alto, CA, USA) with a xenon lamp as the excitation source. The spectra were recorded in the range of 350 to 650 nm, and the excitation wavelength used was 325 nm. For investigating the electrochemical properties of the CQDs/ZnO composite and ZnO array, a three-electrode system was employed. This system included a platinum network counter electrode and an Ag/AgCl (saturated KCl) reference electrode, using a 0.1 mol L<sup>-1</sup> Na<sub>2</sub>SO<sub>4</sub> aqueous electrolyte at 25 °C. To determine the transient photocurrent response, an electrochemical analyzer was used with a 0.5 V bias voltage under light irradiation from a 300 W Xe lamp serving as the light source. Moreover, electron spin resonance (ESR) was employed to evaluate the radical production abilities of the

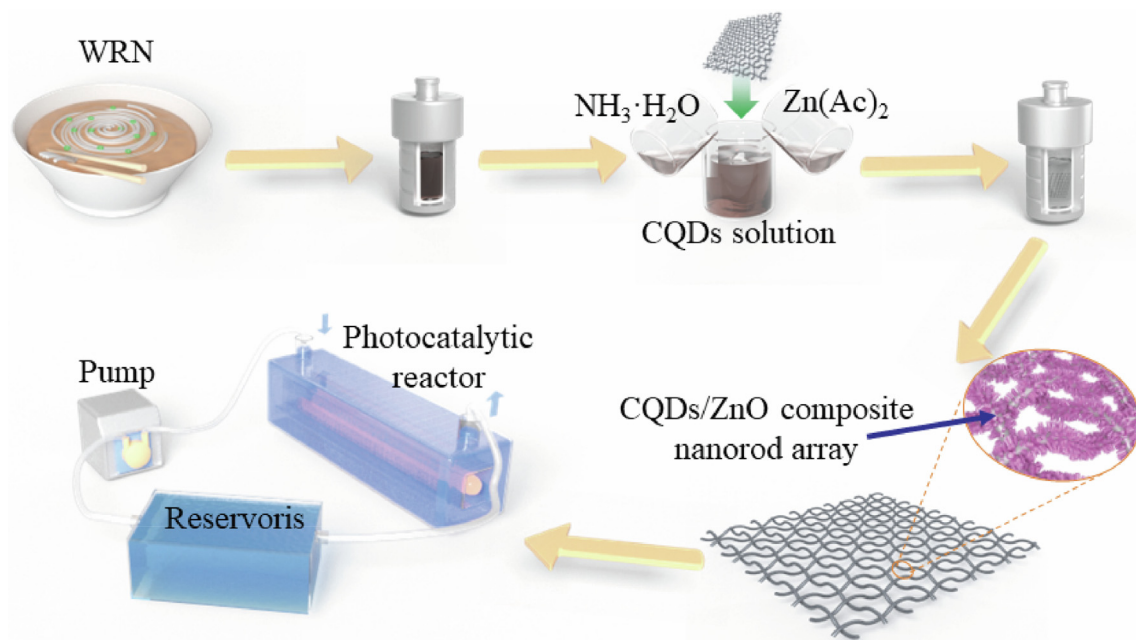


Fig. 1. Schematic illustration of the synthesis and device integration of WRN-based CQDs/ZnO composite nanorod array on steel wire mesh.

**Table 1**  
Synthetic formulation and EDS elemental analysis of CQDs/ZnO composite nanorod array on steel wire mesh.

Serial number	Dosage of CQDs solution (mL)*	Elemental analysis (wt%)		
		Zn	O	C
CQDs/ZnO-1	10	76.90	20.01	3.09
CQDs/ZnO-2	20	72.21	20.91	6.88
CQDs/ZnO-3	30	69.72	20.02	10.26
CQDs/ZnO-4	40	65.29	19.27	15.44
CQDs/ZnO-5	50	62.85	16.43	20.72

\* Dosage of zinc acetate solution and ammonia were 300 mL and 30 mL for all the samples, respectively.

CQDs/ZnO composite array, using an EMXplus X-band electron paramagnetic resonance spectrometer (Bruker, Karlsruhe, Baden-Württemberg, Germany), while dimethyl pyridine N-oxide (DMPO) was served as the spin trapping agent for the ESR measurements.

#### 2.4. Photocatalytic performance measurement

The photocatalytic degradation experiment was conducted in an opaque, closed-loop photocatalytic degradation system, which includes a core photocatalytic reactor, storage reservoir, pumps, and connecting pipes. As shown in Fig. S1, the photocatalytic reactor had dimensions of 1 × 0.2 × 0.2 m. Within the reactor, a blue light tube with a wavelength of 450 nm was installed at the central axis position as the photocatalytic light source. The stainless steel wire mesh with the surface-loaded CQDs/ZnO composite nanorod array was installed above and below the light tube in a wavy pattern, with a ripple spacing of 0.1 m. During operation, the catalytic dye solution (all with a concentration of 20 mg/L) flows through the degradation system at a rate of 80 mL/min. Initially, the blue light tube was not turned on, allowing the solution to undergo dark reactions at room temperature for 1 h. Subsequently, the blue light tube was activated to initiate the photocatalytic process. At specific time points, a small amount of liquid was extracted from the storage reservoir and subjected to spectrophotometric testing after centrifugation. The concentrations of the organic pollutants in the samples were measured by UV-VIS spectrophotometry using a UV3100 UV-VIS-NIR spectrophotometer (Shimadzu, Chiyoda, Tokyo, Japan). Testing wavelengths were as follows: 664 nm (methylene blue), 618 nm (malachite green), 582 nm (methyl violet), 543 nm (basic fuchsin), and 554 nm (rhodamine B). The photocatalytic degradation of organic pollutants was measured with the value of  $C/C_0$ . Each of the photocatalytic degradation results presented in this paper represented the average measurement of three samples having the same composition.

The photocatalytic degradation efficiency of organic pollutants is evaluated by calculating the  $C_t/C_0$  values and could utilize the Langmuir-Hinshelwood model to depict the kinetics of photocatalysis, in which the integral is expressed as:

$$t = \left( \frac{1}{K_r K} \right) \ln \left( \frac{C_0}{C} \right) + \frac{C_0 - C}{K_r} \quad (1)$$

where  $t$  represents the duration of radiation exposure, whose unit is min;  $C_t$  indicates the concentration of organic pollutants at time  $t$ , whose unit is mg/L, whereas  $C_0$  denotes its initial concentration, whose unit is mg/L;  $K$  indicates the equilibrium constant for the adsorption of organic pollutants on the catalyst, whose unit is mol/L; and  $K_r$  is equivalent to the maximum rate of the reaction that can be achieved under the given conditions at the highest possible coverage, whose unit is mol/(L·s).

When the initial level of organic contaminants is low, the second term in Eq. (1) becomes signed and can therefore be ignored. Hence, the kinetic simulations employed for photocatalytic degradation in this paper utilize the following equation:

$$\ln \left( \frac{C_0}{C} \right) = K_r K t = K_{app} t \quad (2)$$

where  $K_{app}$  is the apparent degradation rate constant in  $\text{min}^{-1}$ , used as the basic kinetic parameter.

Furthermore, the obtained CQDs/ZnO array on the steel wire mesh was applied to real water purification. We collected actual river water samples from Nanjing Normal University (NNU) and, upon returning to the laboratory, subjected them to filtration to remove impurities. Subsequently, we employed the CQDs/ZnO array on the steel wire mesh for the purification of the river water sample. To gauge the degradation capacity of photocatalysts towards organic pollutants in the water sample, we utilized the mineralization efficiency of total organic carbon (TOC) as a metric. This assessment involved passing the river water sample through a photocatalytic reactor containing a steel wire mesh loaded with a CQDs/ZnO composite nanorod array, while employing a pure ZnO array as the control. The mineralization efficiency of TOC of river water sample was test using a Multi N/C 3100 TOC analyzer (Analytik Jena, Jena, Germany).

### 3. Results and discussion

#### 3.1. Structural characterization

The microscopic morphology of CQDs/ZnO composite nanorod arrays, as well as the pure ZnO array on the steel wire mesh, was investigated using SEM, and the results are presented in Fig. 2. As shown in Fig. 2a, in the absence of CQDs, the hydrothermal reaction of zinc acetate and ammonia could still form a pure ZnO array on the surface of the steel wire mesh. However, the resulting ZnO array displayed poor regularity, with elongated rod-like clusters and numerous irregularly arranged secondary crystals. In contrast, the introduction of CQDs significantly altered the morphology of the ZnO-based array on the steel wire mesh. At relatively low CQDs loading levels (such as CQDs/ZnO-1 and CQDs/ZnO-2 samples), the CQDs/ZnO particles on the stainless steel wire mesh were irregularly distributed in a spherical manner, failing to form a regular array (See Fig. 2b and 2c). With a moderate loading of CQDs, a regular hexagonal prism array distribution was achieved (CQDs/ZnO-3 sample, see Fig. 2d) on the stainless steel wire mesh. However, excessive CQDs loading led to the occurrence of clustering phenomenon in the array, and the array exhibited a cauliflower-like appearance (CQDs/ZnO-4 sample, Fig. 2e). When the loading amount of carbon reached 20.72 wt% (CQDs/ZnO-5 sample, Fig. 2f), a layer of CQDs/ZnO composite on the steel wire mesh was clearly observed, but a well-organized nano array was no longer discernible. In summary, CQDs played a crucial role in modulating the morphology of the ZnO-based array. The addition of an appropriate amount of CQDs (e.g., CQDs/ZnO-3 sample, see Fig. 2d) effectively reduced the secondary crystallization of ZnO, resulting in a more uniform CQDs/ZnO array comprising a large number of relatively thick and short hexagonal crystals. This arrangement

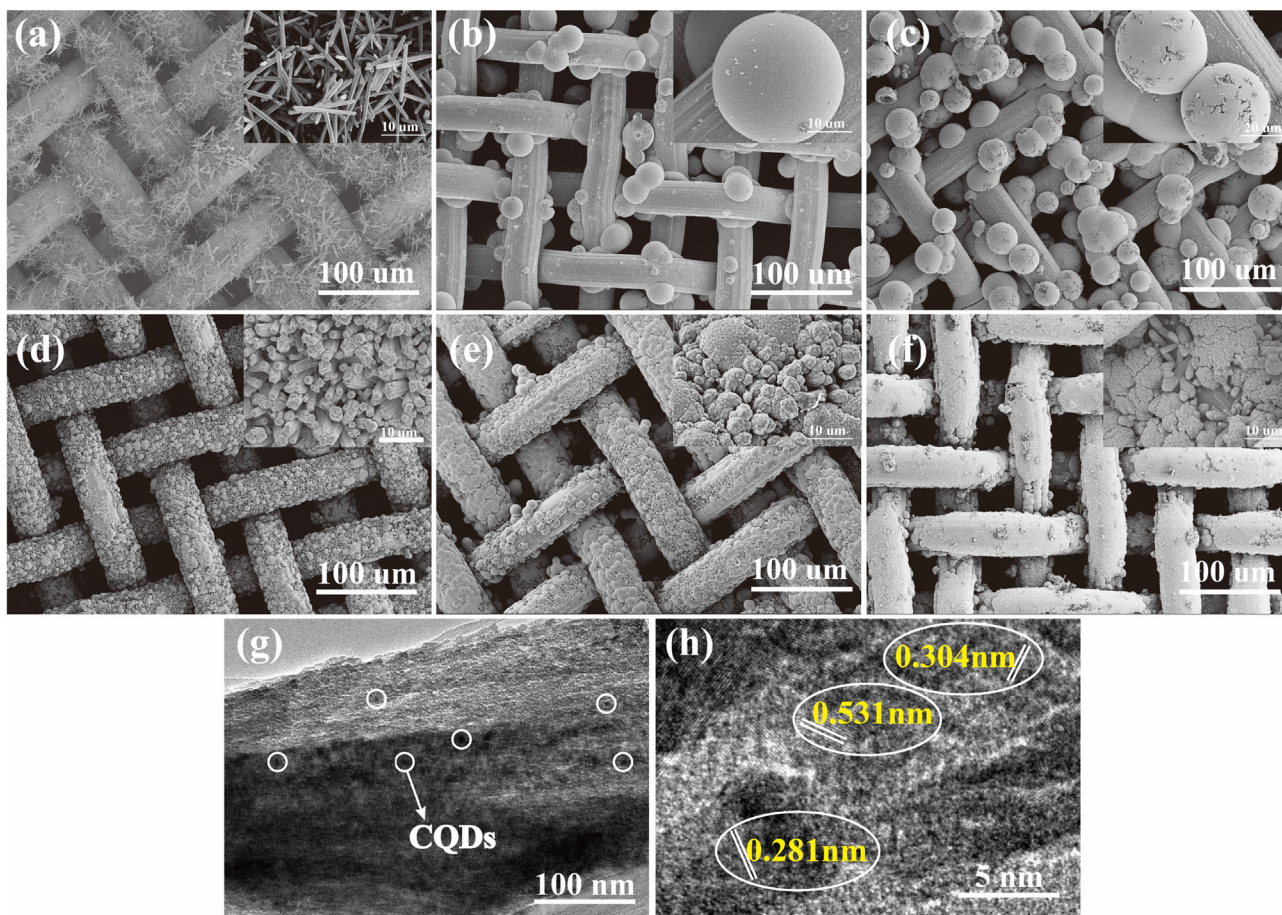


**Fig. 2.** (a–f) SEM images of pure ZnO array (a) and CQDs/ZnO-*x* arrays [*x* = 1 (b), 2 (c), 3 (d), 4 (e) and 5 (f)] on steel wire mesh; (g–h) The TEM (g) and HRTEM (h) images of CQDs/ZnO-3 sample.

was found to be beneficial for achieving excellent photocatalytic performance.

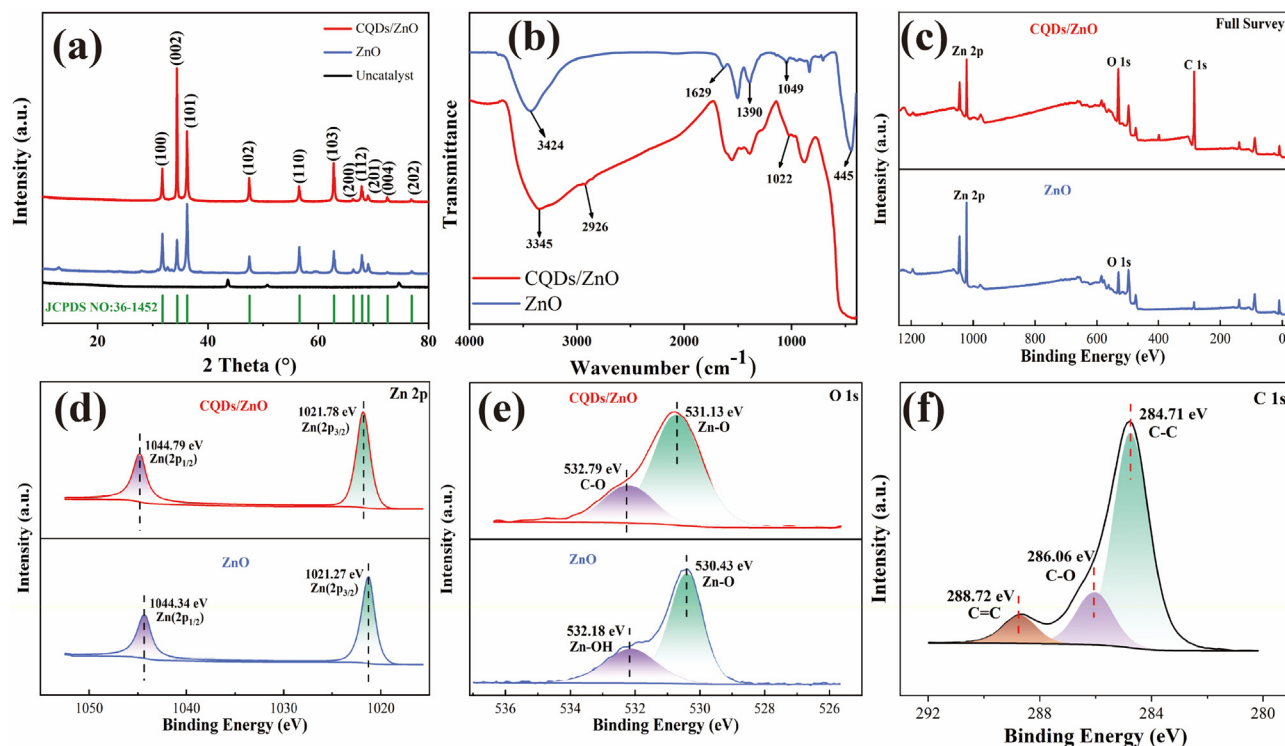
Fig. 2g and h depict the TEM images of the CQDs/ZnO-3 composite. The CQDs/ZnO composite showed a columnar structure, and spheroidal particles of CQDs were uniformly distributed on the surface of ZnO (Fig. 2g). The HRTEM image (See Fig. 2h) displayed both the lattice interleaving of nano ZnO and CQDs. The lattice stripes of 0.531 nm and 0.304 nm corresponded to the (204) and (110) crystallographic planes of hexagonal ZnO, respectively. Additionally, the (020) lattice plane of CQDs was observed with a lattice spacing of 0.281 nm. Furthermore, the element mapping shows that the distribution of CQDs on the ZnO surface is relatively uniform, with a carbon content of 10.26 wt% in the composite (See Fig. 4f).

Fig. 3a illustrates the PXRD patterns of the CQDs/ZnO composite and pure ZnO powder. The two PXRD spectra exhibited similar peaks, while the diffraction peak of CQDs could not be observed obviously in the CQDs/ZnO composite, mainly due to its relatively low carbon content (10.26 wt%) and low crystallinity. Intense diffraction peaks could be observed at  $2\theta = 31.76^\circ, 34.41^\circ, 36.25^\circ, 47.53^\circ, 56.59^\circ, 62.85^\circ, 66.37^\circ, 69.08^\circ, 72.55^\circ, \text{ and } 76.95^\circ$ , corresponding to the (100), (002), (101), (102), (110), (103), (200), (112), (201), (004), and (202) crystalline planes of the hexagonal fibrous ZnO phase (JCPDS card no. 36–1451), respectively.

In the IR spectrum of the CQDs/ZnO composite shown in Fig. 3b, the characteristic absorption peaks of CQDs were observed. These included vibrations related to the stretching of the hydroxyl O–H

bond ( $3345\text{ cm}^{-1}$ ), the C–H bond ( $2926\text{ cm}^{-1}$ ), and the C–O bond ( $1049\text{ cm}^{-1}$ ). When compared with the IR spectrum of pure ZnO, the incorporation of CQDs caused a redshift and narrowing of the solid Zn–O vibrations at  $445\text{ cm}^{-1}$ . This phenomenon could be attributed to the reaction between the carboxyl group present in the CQDs and the hydroxyl groups on the surface of ZnO.

Fig. 3c–f and Table 2 display the XPS spectra for the CQDs/ZnO-3 composite and pure ZnO. The results demonstrated the presence of Zn, C, and O elements. The distinctive peaks at 1021.78 and 1044.79 eV in the Zn 2p high-resolution spectra corresponded to the signals of Zn 2p<sub>3/2</sub> and Zn 2p<sub>1/2</sub>, respectively. In the high-resolution spectra of the O 1s orbital, Zn–O and C–O bonds were observed in the CQDs/ZnO composites with distinctive signals at 531.13 eV and 532.79 eV, respectively. For pure ZnO, the O 1s high-resolution spectra had two characteristic peaks at 530.43 eV and 532.18 eV, attributed to Zn–O bonding and the hydroxyl group on the surface of ZnO, respectively. Additionally, the characteristic peaks at 284.71 eV in the C 1s high-resolution spectra were associated with C–C bonds of CQDs, and the peaks at 286.06 eV and 288.72 eV were attributed to the C–O and C=C bonds, respectively. Combining the FT-IR analysis, it was speculated that the interaction between the carboxyl group of CQDs and the hydroxyl group on the surface of ZnO resulted in a closer connection between them. The hydroxyl signal on the surface of ZnO vanished, while a signal for the C–O bond was produced simultaneously. These observations indicated the successful preparation of the CQDs/ZnO composite array.



**Fig. 3.** (a–b) The PXRD spectra (a) and FT-IR spectra (b) of the resulted CQDs/ZnO composite array and pure ZnO array. (c–f) The full XPS spectra (c), high-resolution XPS spectra of Zn 2p (d), O 1s (e) and C 1s (f, CQDs/ZnO composite array only) of the resulted CQDs/ZnO composite array and pure ZnO array.

**Table 2**

XPS peak assignments of CQDs/ZnO composite array and pure ZnO array.

Photocatalysts	Element	Peak (eV)	Surface Group	Identification
CQDs/ZnO composite array	Zn 2p	1044.79	Zn–O	Zn(2p <sub>1/2</sub> )
		1021.78	Zn–O	Zn(2p <sub>3/2</sub> )
	C 1s	284.71	C	Graphitic carbon
		286.06	C–O	Presence of an alcoholic or etheric functional group in CQDs.
		288.72	C=C	Conjugated $\pi$ -electrons in the aromatic ring of CQDs.
O 1s	531.13	Zn–O	Zinc bonded with oxygen.	
	532.79	C–O	CQDs singly bonded with oxygen.	
Pure ZnO array	Zn 2p	1044.34	Zn–O	Zn(2p <sub>1/2</sub> )
		1021.27	Zn–O	Zn(2p <sub>3/2</sub> )
	O 1s	530.43	Zn–O	Oxygen bonded to zinc
		532.18	O–H	Hydroxyl groups on ZnO surfaces

### 3.2. Photocatalytic performance

We investigated the photocatalytic activities of the resulting CQDs/ZnO composite arrays as well as the pure ZnO array in on steel wire mesh, using methylene blue as the substrate for degradation under 450 nm visible blue light. As depicted in Fig. 4a–c, the photodegradation of methylene blue using pure ZnO arrays without CQDs was very low, exhibiting a degradation efficiency of only 10.52% in 90 min and a kinetic constant of  $0.963 \times 10^{-3} \text{ min}^{-1}$ . However, upon introducing an appropriate amount of CQDs, the degradation efficiency of the CQDs/ZnO composite on methylene blue was significantly improved. Among the CQDs/ZnO composites with different CQDs loadings, the composite with approximately 10.26 wt% carbon content (CQDs/ZnO-3 sample) exhibited the highest degradation efficiency and achieved complete degradation of methylene blue within 90 min, showing a degradation efficiency of 99.4% and a high kinetic constant of  $33.5 \times 10^{-3} \text{ min}^{-1}$ . Notably, this kinetic constant was 37 times

higher than that of the pure ZnO array. Combining our previous research findings (Jin et al., 2022b) with the results of microscopic morphology, we observed that a moderate amount of CQDs loading (approximately 10 wt%), and a uniform hexagonal crystal cluster array could contribute to the enhancement of photocatalytic efficiency. In comparison to the CQDs/ZnO-3 sample, other CQDs/ZnO composite arrays with excessive or insufficient CQDs loading failed to achieve complete degradation of methylene blue pollutants within 90 min of illumination. This outcome could be attributed to their insufficiently regular particle arrangement and the shielding effect caused by excessive carbon content.

Compared to other CQDs/ZnO powder catalysts, the CQDs/ZnO composite array on the stainless steel wire mesh offered the convenience of easy processing into photocatalytic devices or components, capable of stable operation over an extended period and adapting to repeated cyclic degradation processes, without the need for cumbersome recycling and reprocessing procedures. Fig. 4d illustrates the outcomes of the photocatalyst reusability test

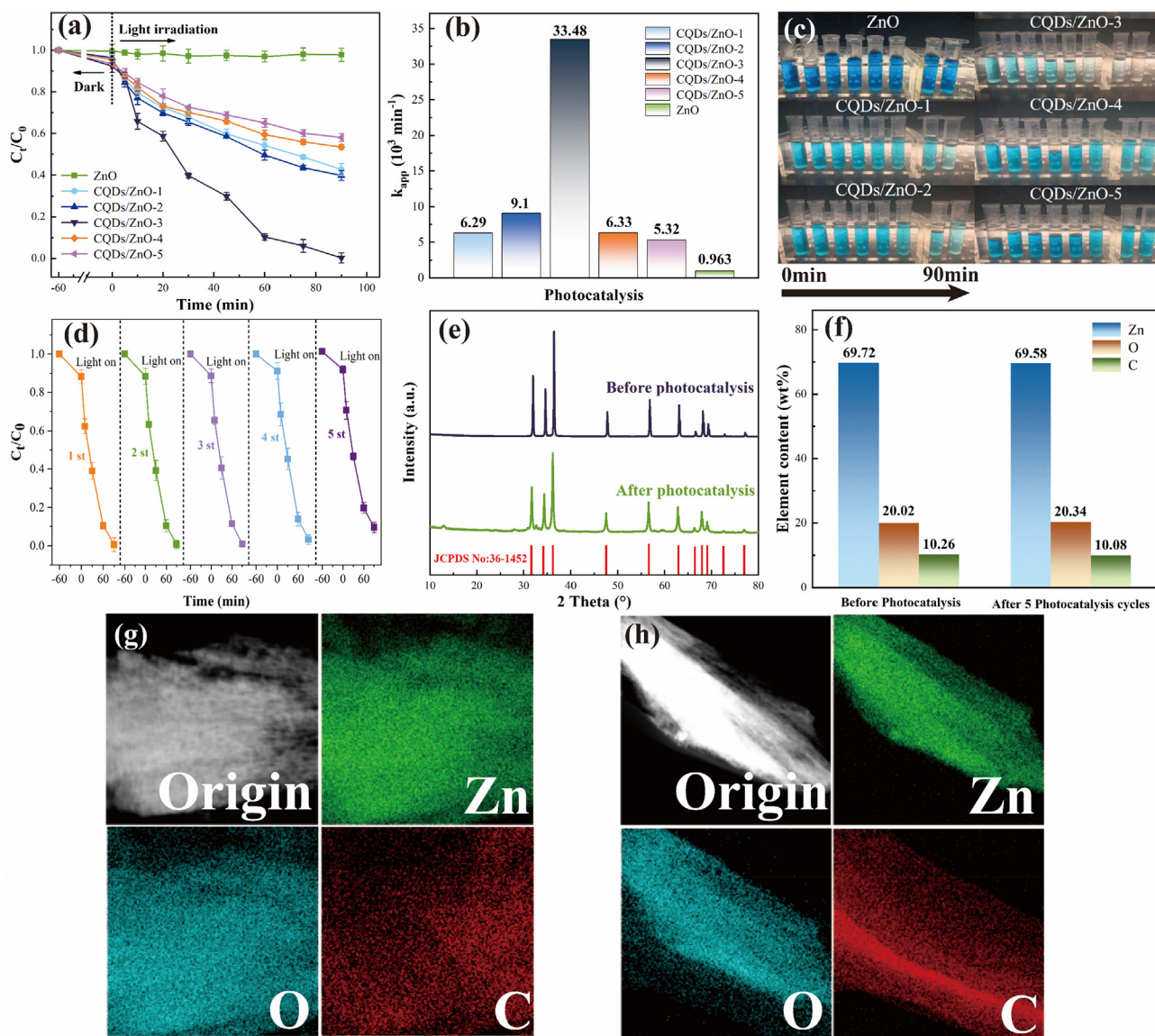


**Fig. 4.** (a–b): The photocatalytic degradation rate within different irradiation times (a) and apparent degradation rate constant ( $k_{app}$ , b) of CQDs/ZnO composite arrays (CQDs/ZnO- $x$ ,  $x = 1, 2, 3, 4$  and 5) and pure ZnO array to methylene blue under 450 nm blue light. (c) The photographs showing the photocatalytic degradation effects on methylene blue of CQDs/ZnO composite arrays (CQDs/ZnO- $x$ ,  $x = 1, 2, 3, 4$  and 5) and pure ZnO array. (d) The photocatalytic degradation rate of CQDs/ZnO composite array (CQDs/ZnO-3 sample) of the different photocatalytic cycle with 90 min as a working cycle. (e) The PXRD patterns of CQDs/ZnO-3 sample before photocatalysis and after five photocatalysis cycles. (f) The elemental content of CQDs/ZnO-3 sample before photocatalysis and after five photocatalysis cycles. (g–h) elemental mapping of CQDs/ZnO-3 sample before photocatalysis (g) and after five photocatalysis cycles (h).

of CQDs/ZnO array (CQDs/ZnO-3 sample). Remarkably, after undergoing five successive cycles, the CQDs/ZnO array demonstrated remarkable stability in its degradation rate towards methylene blue, maintaining an efficiency of over 95%. Moreover, the CQDs/ZnO composite array ensured its structural and property stability during the photocatalytic process. As evident from the PXRD patterns in Fig. 4e, the CQDs/ZnO composite array before and after five photocatalytic cycles remained nearly identical. The EDS mapping revealed that even after five photocatalytic cycles, the CQDs were still evenly distributed on the surface of ZnO within the CQDs/ZnO composite array. Simultaneously, the carbon content remained at 10.08 wt%, indicating no significant loss compared to the original sample (see Fig. 4f–h).

Apart from methylene blue, the resulted CQDs/ZnO composite array (CQDs/ZnO-3 sample) also displayed a high efficient photocatalytic degradation effect on other common water-soluble dyes such as malachite green, methyl violet, basic fuchsin, and rho-

damine B under visible light irradiation, and showed much better photocatalytic performance than that of pure ZnO array. Similar to the photocatalytic degradation of methylene blue, the CQDs/ZnO-3 sample exhibited the highest degradation efficiency among the CQDs/ZnO composites with different CQDs loadings, and achieved high degradation efficiency of 100%, 100%, 96.2% and 83.3% for malachite green, basic magenta, rhodamine B and methyl violet, respectively (See Table 3 and Fig. S3 in ESI). Compared with other previously reported ZnO-based nanocomposite arrays, the waste rice noodle-based CQDs/ZnO composite nanorod array on a steel wire mesh exhibited higher catalytic efficiency for multiple pollutants, capable of visible-light photocatalytic degradation (See Table 3). Additionally, due to the use of inexpensive waste rice noodle-based CQDs as components and a steel wire mesh as the substrate, the fabrication cost was significantly reduced, enabling effective utilization of waste resources and displaying high environmental friendliness. Consequently, this approach showed

**Table 3**  
Photocatalytic degradation effect of different ZnO-based nanocomposite arrays.

Composite	Substrate	Excitation source	Pollutant	Irradiation times (min)	Degradation rate (%)	Reference
CQDs/ZnO	PVDF	A single-channel peristaltic pump (100 rpm/min)	Tetracycline (TC)	70	39.78	(Wang et al., 2023)
CQDs/ZnO	Nanofiber membranes	An UV lamp (250 W, 365 nm) and natural sunlight	MB	180	92.08	(Xu et al., 2023)
rGO/ZnO	rGO nanosheets	A UV lamp	Cr(VI)	40	47	(Xia et al., 2020)
CuO NPs/ZnO	A clean ITO substrate	A Xe lamp (CEL-S500)	MO	60	44	(Zhang et al., 2019)
rGO@ZnO	NH <sub>3</sub> processed chemically converted rGO nanosheets	A UV light source (100 W)	Ofloxacin	300	99	(Sharma et al., 2020)
CQDs/ZnO array based on WRN	Stainless steel wire mesh	Visible light ( $\lambda = 450$ nm)	Methylene Blue	90	99.4	This work
			Malachite Green		100	
			Basic Magenta		100	
			Rhodamine B		96.2	
			Methyl Violet		83.3	

promising potential for large-scale industrial wastewater treatment applications.

Furthermore, the obtained CQDs/ZnO array on the steel wire mesh was applied to real water purification. The total organic carbon (TOC) refers to the total amount of organic substances in water, including dissolved and particulate organic matter. Photocatalysts can oxidize organic pollutants into harmless substances such as CO<sub>2</sub> and H<sub>2</sub>O. Therefore, the mineralization efficiency of TOC can be used to measure the degradation capability of photocatalysts towards organic pollutants in natural water bodies. A higher mineralization efficiency indicates that organic pollutants are more effectively decomposed and removed during the photocatalytic process. The mineralization efficiency was assessed by passing a river water sample through a photocatalytic reactor containing steel wire mesh loaded with CQDs/ZnO composite nanorod array, while using pure ZnO array as the control. As shown in Fig. 5a, after a photocatalytic process of 90 min, the CQDs/ZnO composite nanorod array achieved a high mineralization efficiency of up to 48%, while the pure ZnO array only reached 11%. Moreover, the leaching rate of Zn during the 90 min catalytic process was only 1.2%, indicating that the CQDs/ZnO composite nanorod array on the steel wire mesh could be applied in practical large-scale water purification projects, demonstrating long-lasting effectiveness in degrading water-soluble pollutants (See Fig. 5b).

### 3.3. Photocatalytic mechanism

The light absorption range is a critical factor that influences the catalytic activity of photocatalysts. The UV-VIS absorption spectra

of CQDs, pure ZnO, and the CQDs/ZnO composite are examined and depicted in Fig. 6a. Pure ZnO displayed strong absorption in the UV range (below 384 nm) but showed low absorption in the visible region (beyond 420 nm). However, upon introducing CQDs to form the CQDs/ZnO composite, the absorption strength was significantly elevated within the visible spectrum of 400–800 nm. This demonstrated that the presence of CQDs greatly enhanced ZnO's ability to utilize visible light energy, resulting in improved energy capture and generation of electron-hole pairs when exposed to visible light. Furthermore, the band gaps of the CQDs/ZnO composite and the pure ZnO array were determined using the Kubelka-Munk method. As depicted in Fig. 6b, the presence of CQDs in the composite system resulted in a narrower band gap (1.35 eV) compared to the pure ZnO array with a band gap of approximately 3.15 eV. This facilitated electron hopping, leading to enhanced photocatalytic degradation performance.

XPS valence band spectroscopy was employed to determine the valence band potentials (VB) of both the CQDs/ZnO composite and pure ZnO array. As illustrated in Fig. 6c, for pure ZnO, the VB value (2.74 eV) exceeded E<sup>0</sup> ( $\cdot\text{OH}$ , H<sup>+</sup>/H<sub>2</sub>O) (2.38 eV vs. NHE), while its conduction band potential (CB) could reach -0.41 eV (E<sub>CB</sub> = E<sub>VB</sub> - E<sub>g</sub>), which was more negative than E<sup>0</sup>(O<sub>2</sub>/O<sub>2</sub><sup>-</sup>) (-0.33 eV vs. NHE). This indicated that the photogenerated holes of the ZnO array could oxidize H<sub>2</sub>O, producing hydroxyl radicals ( $\cdot\text{OH}$ ), while its photogenerated electrons could reduce O<sub>2</sub>, generating superoxide radicals (O<sub>2</sub><sup>-</sup>). By contrast, the CQDs/ZnO composite array exhibited a valence band potential of 2.98 eV, higher than that of ZnO (2.74 eV), enabling better oxidation of H<sub>2</sub>O to form photocatalytically  $\cdot\text{OH}$  radicals. By combining its own band gap (1.35 eV) with

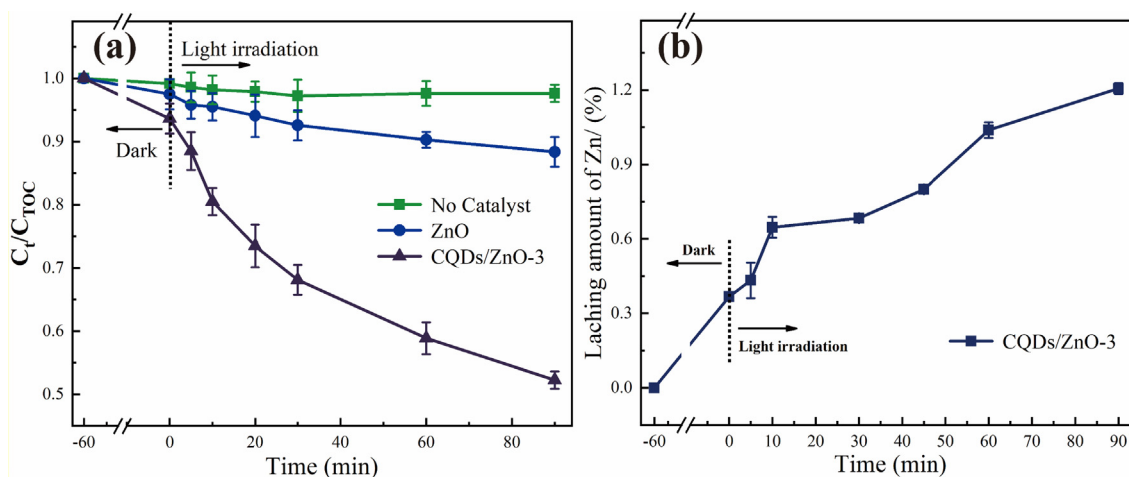


**Fig. 5.** (a) The mineralization efficiency of TOC of river water sample using CQDs/ZnO composite array and pure ZnO array as photocatalysts within different irradiation times; (b) the leaching rate of Zn of CQDs/ZnO composite array within different irradiation times.

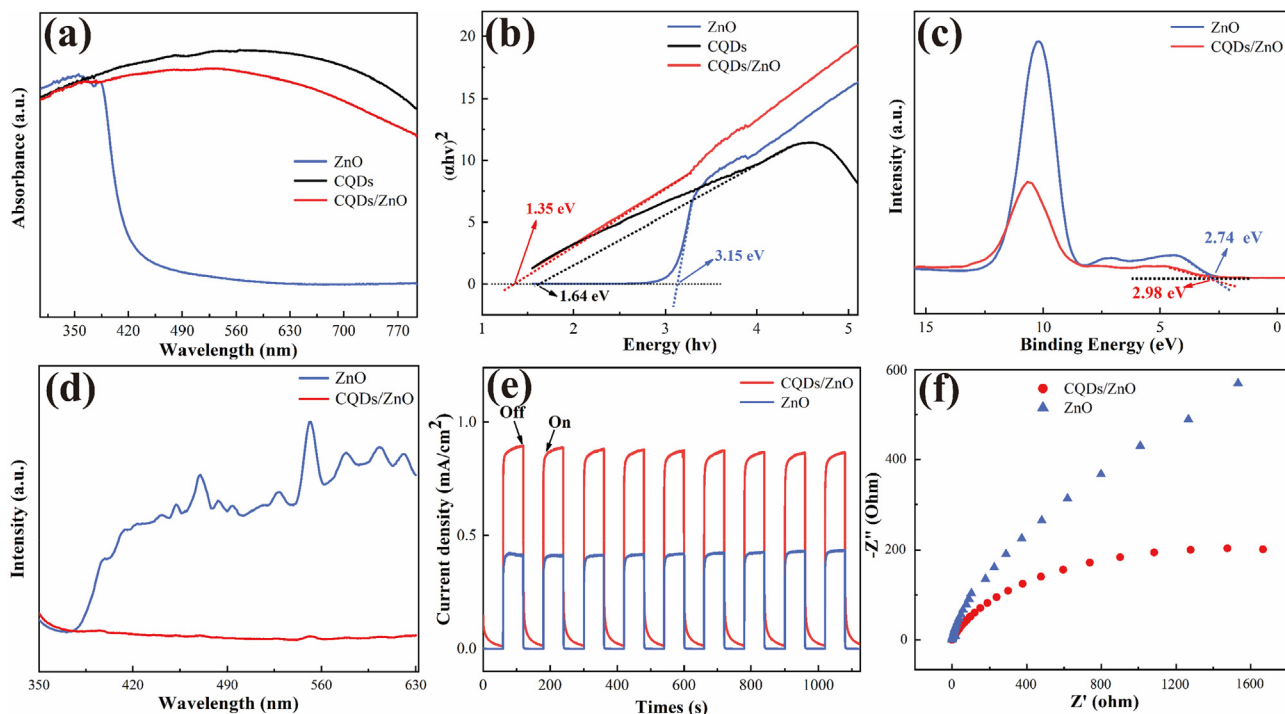


**Fig. 6.** (a–b) The UV–VIS absorption spectra (a) and Tauc plots (b) for CQDs/ZnO composite, pure ZnO array and CQDs powder; (c–f) The XPS valence band spectra (c), photoluminescence spectra (d), photocurrent response (e) and electrochemical impedance spectra (f) for CQDs/ZnO composite and pure ZnO array.

the band gap of CQDs (1.64 eV), its CB potential was calculated to be  $-0.46$  eV, which was lower than  $E^0(\text{O}_2/\text{O}_2^-)$  ( $-0.33$  eV vs. NHE). This indicated that the CQDs/ZnO composite array could reduce oxygen in water, generating photocatalytically active  $\text{O}_2^-$  radicals.

The introduction of CQDs significantly improved the defects in ZnO photocatalysis, and this positive effect was further confirmed through fluorescence spectroscopy tests. As shown in Fig. 6d, compared to pure ZnO array, the fluorescence emission intensity of the CQDs/ZnO composite array was notably lower, indicating the effective modification of CQDs in reducing the recombination of electron-hole pairs. This advantage of the CQDs/ZnO composite array was also validated by the photocurrent response under visible light irradiation on/off (Fig. 6e). It was evident that the photocurrent of the array was significantly enhanced after the introduction of CQDs, implying a faster charge transfer at the electron acceptor interface from CQDs to ZnO, thus leading to a more efficient separation of electron-hole pairs. Furthermore, electrochemical impedance spectra showed that the half-circle diameter of CQDs/ZnO composite array was notably smaller than that of pure ZnO (Fig. 6f), indicating higher electron migration efficiency and lower charge transfer resistance. These results were consistent with the findings from photoluminescence and photocurrent tests.

The ability of the CQDs/ZnO composite array to generate radicals for photocatalysis under light irradiation was investigated via electron spin resonance spectroscopy (ESR) employing 5,5-dimethyl-1-pyrrolo N-oxide (DMPO) as a spin-trapping reagent. As illustrated in Fig. 7a–b, the CQDs/ZnO composite array could produce  $\text{O}_2^-$  and  $\cdot\text{OH}$  radicals and therefore could degrade aqueous organic pollutants. Fig. 7c illustrated a plausible mechanism for methylene blue removal over the CQDs/ZnO composite array on steel wire mesh. Under exposure to visible light, the CQDs/ZnO composite array was more susceptible to excitation through photogenerated electrons in the CB, thus leaving holes in the VB. The accession of CQDs enhanced the absorption of visible light energy and resulted in a more effective separation of electron-hole pairs,

leading to more photogenerated electrons for the reduction of  $\text{O}_2$  and more photogenerated holes for the oxidation of  $\text{H}_2\text{O}$ . The photogenerated holes initiated a reaction with  $\text{H}_2\text{O}$ , resulting in the production of  $\cdot\text{OH}$  radicals, while the electrons separated on the CQDs triggered a reaction with  $\text{O}_2$  to generate  $\text{O}_2^-$  radicals. The resulting  $\text{O}_2^-$  and  $\cdot\text{OH}$  radicals generated could decompose MB to  $\text{CO}_2$  and  $\text{H}_2\text{O}$ , thus resulting in excellent photocatalytic activity.

#### 4. Conclusions

In this work, WRN-based CQDs/ZnO composite nanorod array on steel wire mesh was designed and synthesized for the first time, which resulted in a photocatalytic device which offers advantages of highly efficient photocatalytic degradation, lower production costs, convenient assembly, good recyclability and environmental friendliness. The result showed that, the incorporation of CQDs derived from WRN played a crucial role in controlling the morphology of the ZnO-based array. This could potentially serve as a cost-effective method for controlling the morphology of nanomaterials. By optimizing the loading of CQDs, the CQDs/ZnO composite array achieved a regular hexagonal prism nanorod array distribution and exhibited highly efficient photocatalytic degradation of various organic pollutants, including methylene blue, malachite green, methyl violet, basic fuchsin, and rhodamine B, which showed better photocatalytic performance than pure ZnO array. For instance, in the case of methylene blue, the CQDs/ZnO composite demonstrated a remarkable degradation rate of 99.4% within 90 min, with a high degradation rate constant of  $0.033 \text{ min}^{-1}$ . Moreover, the composite material could be recycled and reused for five photocatalytic cycles without a significant decrease in its degradation performance. Additionally, this CQDs/ZnO composite array could be applied to real water purification with high mineralization efficiency. The introduction of CQDs based on WRN to ZnO array could result in efficient electron-hole pair separation and enable more

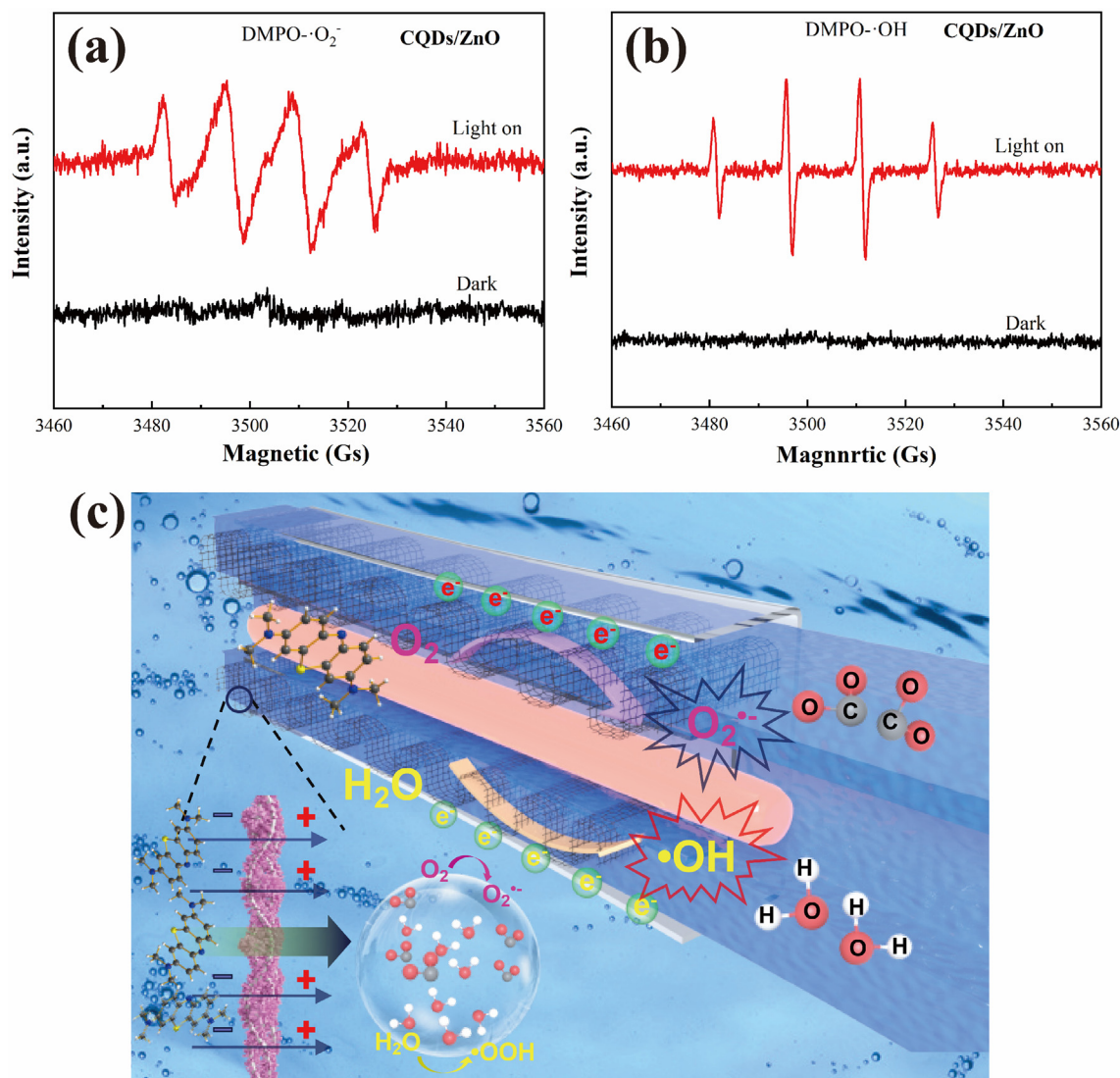


**Fig. 7.** (a–b) DMPO spin-trapping ESR spectra of CQDs/ZnO composite array in water (a) and methanol (b) under visible light irradiation; (c) a diagrammatic representation of the photochemical catalysis mechanism for CQDs/ZnO composite array on steel wire mesh.

photogeneration electrons to reduce  $O_2$  and more photogeneration holes to oxidize  $H_2O$ , which could cause stronger abilities in producing  $O_2^-$  and  $\cdot OH$  radicals and better photocatalytic activity.

Compared with other powdered photocatalysts, the implementation of the WRN-based CQDs/ZnO composite nanorod array on steel wire mesh in this study effectively addresses the challenges of recycling and assembling powdered catalysts, which hinder their application in continuous, large-scale industrial water purification projects. Due to the relatively low cost of WRN-based CQDs and steel wire mesh, the photocatalytic degradation efficiency of the CQDs/ZnO composite nanorod array on steel wire mesh offers the advantages of being cost-effective, readily available raw materials, and environmentally friendly, making it a potential candidate for constructing low-cost photocatalytic water purifier. This array is also expected to be used for photocatalytic hydrogen production or carbon dioxide reduction. Furthermore, compared with other recycling methods for catering waste, the conversion strategy of WRN to CQDs/ZnO composite nanorod array on steel wire mesh can add higher value, presenting promising prospects for industrialization and providing a novel approach for the recycling of cooking waste. However, the CQDs/ZnO composite nanorod array on steel wire mesh reported in this study has not yet been applied

in large-scale industrial water treatment projects. Therefore, further research is needed to investigate the material's long-term photocatalytic performance, stability, and corrosion resistance under extended exposure to light. In addition, the potential application of the obtained CQDs/ZnO composite array in photocatalytic hydrogen production or carbon dioxide reduction still requires further validation.

#### CRediT authorship contribution statement

**Ruijie Che:** Conceptualization, Methodology, Data curation, Writing – original draft. **Biyang Tu:** Methodology, Data curation, Writing – original draft. **Yining Zhu:** Software, Writing – review & editing. **Jiahe Miao:** Data curation, Supervision. **Xinyan Jin:** Validation. **Shuoping Chen:** Funding acquisition, Project administration, Supervision, Writing – review & editing.

#### Declaration of Competing Interest

The authors declare that they have no known competing financial interests or personal relationships that could have appeared to influence the work reported in this paper.

## Acknowledgments

This work was supported by grants from the National Nature Science Foundation of China (No. 51763007), Guangxi Natural Science Foundation Program (No. 2015GXNSFBA139033), and the Sharing Foundation of Guangxi Key Laboratory of Optical and Electronic Materials and Devices (No. 20 AA-9).

## Appendix A. Supplementary material

Supplementary data to this article can be found online at <https://doi.org/10.1016/j.arabj.2023.105231>. Fig. S1: Schematic diagram of the photocatalytic reactor; Fig. S2: Pseudo-first-order kinetic fitting of photocatalytic degradation of CQDs/ZnO composite arrays and pure ZnO array to methylene blue; Fig. S3: Photocatalytic degradation rate of CQDs/ZnO composite arrays and pure ZnO array to malachite green, basic magenta, rhodamine B and methyl violet.

## References

- Abd-Elrahim, A.G., Chun, D.-M., 2021. Room-temperature deposition of ZnO-graphene nanocomposite hybrid photocatalysts for improved visible-light-driven degradation of methylene blue. *Ceram. Int.* 47, 12812–12825. <https://doi.org/10.1016/j.ceramint.2021.01.142>.
- Abdollahi, B., Najafidoust, A., Abbasi Asl, E., Sillanpaa, M., 2021. Fabrication of ZIF-8 metal organic framework (MOFs)-based CuO-ZnO photocatalyst with enhanced solar-light-driven property for degradation of organic dyes. *Arab. J. Chem.* 14. <https://doi.org/10.1016/j.arabj.2021.103444>.
- Arumugham, T., Alagumuthu, M., Amimodu, R.G., Munusamy, S., Iyer, S.K., 2020. A sustainable synthesis of green carbon quantum dot (CQD) from *Catharanthus roseus* (white flowering plant) leaves and investigation of its dual fluorescence responsive behavior in multi-ion detection and biological applications. *Sustain. Mater. Technol.* 23, e00138.
- Barik, S., Paul, K.K., 2017. Potential reuse of kitchen food waste. *J. Environ. Chem. Eng.* 5, 196–204. <https://doi.org/10.1016/j.jece.2016.11.026>.
- Behnood, R., Sodeifian, G., 2020. Synthesis of N doped-CQDs/Ni doped-ZnO nanocomposites for visible light photodegradation of organic pollutants. *J. Environ. Chem. Eng.* 8. <https://doi.org/10.1016/j.jece.2020.103821>.
- Chang, P., Wang, Y.H., Wang, Y., Zhu, Y., 2022. Current trends on In<sub>2</sub>O<sub>3</sub> based heterojunction photocatalytic systems in photocatalytic application. *Chem. Eng. J.* 450. <https://doi.org/10.1016/j.cej.2022.137804>.
- Chen, H., Yuan, X., Jiang, L., Wang, H., Zeng, G., 2022. Highly efficient As(III) removal through simultaneous oxidation and adsorption by N-CQDs modified MIL-53 (Fe). *Sep. Purif. Technol.* 286. <https://doi.org/10.1016/j.seppur.2021.120409>.
- Chiu, Y.-H., Chang, T.-F., Chen, C.-Y., Sone, M., Hsu, Y.-J., 2019. Mechanistic insights into photodegradation of organic dyes using heterostructure photocatalysts. *Catalysts* 9, 430. <https://doi.org/10.3390/catal9050430>.
- Chu, Z., Wang, W., Zhou, A., Huang, W.-C., 2019. Charging for municipal solid waste disposal in Beijing. *Waste Manag.* 94, 85–94. <https://doi.org/10.1016/j.wasman.2019.05.051>.
- Gangu, K.K., Maddila, S., Jonnalagadda, S.B., 2019. A review on novel composites of MWCNTs mediated semiconducting materials as photocatalysts in water treatment. *Sci. Total Environ.* 646, 1398–1412. <https://doi.org/10.1016/j.scitotenv.2018.07.375>.
- Gao, W., Liu, Y., Dong, J., 2021. Immobilized ZnO based nanostructures and their environmental applications. *Prog. Nat. Sci.: Mater. Int.* 31, 821–834. <https://doi.org/10.1016/j.pnsc.2021.10.006>.
- Han, Y., Han, Y., Du, G., Zhang, T., Guo, Q., Yang, H., Li, R., Xu, Y., 2021. Physiological effect of colloidal carbon quantum dots on *Bursaphelenchus xylophilus*. *RSC Adv.* 11, 6212–6220. <https://doi.org/10.1039/D0RA10144C>.
- Huang, H., Xue, Y., Xie, Y., Yang, Y., Yang, L., He, H., Jiang, Q., Ying, G., 2022. MoS<sub>2</sub> quantum dot-decorated MXene nanosheets as efficient hydrogen evolution electrocatalysts. *Inorg. Chem. Front.* 9, 1171–1178. <https://doi.org/10.1039/D1QJ01528A>.
- Huszla, K., Wysokowski, M., Zgola-Grzeškowiak, A., Staszak, M., Janczarek, M., Jesionowski, T., Wyrwas, B., 2022. UV-light photocatalytic degradation of non-ionic surfactants using ZnO nanoparticles. *Int. J. Environ. Sci. Technol.* 19, 173–188. <https://doi.org/10.1007/s13762-021-03160-1>.
- Jiang, Z., Cheng, B., Zhang, Y., Wageh, S., Al-Ghamdi, A.A., Yu, J., Wang, L., 2022b. S-scheme ZnO/WO<sub>3</sub> heterojunction photocatalyst for efficient H<sub>2</sub>O<sub>2</sub> production. *J. Mater. Sci. Technol.* 124, 193–201. <https://doi.org/10.1016/j.jmst.2022.01.029>.
- Jiang, X., Huang, L., Li, J., Zhang, L., Guo, X., Li, Y., Sun, X., 2021. A novel strategy to construct the superior performance of 3D multi-shell CeO<sub>2</sub>/ZnO@ZnS as a reusable sunlight-driven ternary photocatalyst for highly efficient water remediation. *J. Environ. Chem. Eng.* 9. <https://doi.org/10.1016/j.jece.2021.105608>.
- Jiang, Y., Wang, J., Liu, B., Jiang, W., Zhou, T., Ma, Y., Che, G., Liu, C., 2022a. Superhydrophilic N, S, O-doped Co/CoO/Co<sub>9</sub>S<sub>8</sub>@carbon derived from metal-organic framework for activating peroxydisulfate to degrade sulfamethoxazole: Performance, mechanism insight and large-scale application. *Chem. Eng. J.* 446. <https://doi.org/10.1016/j.cej.2022.137361>.
- Jin, X., Che, R., Yang, J., Liu, Y., Chen, X., Jiang, Y., Liang, J., Chen, S., Su, H., 2022a. Activated carbon and carbon quantum dots/titanium dioxide composite based on waste rice noodles: simultaneous synthesis and application in water pollution control. *Nanomaterials* 12, 472. <https://doi.org/10.3390/nano12030472>.
- Jin, X.-Y., Ying, W.-Y., Che, R.-J., Xiao, P., Zhou, Y.-Q., Liu, Y., Liu, M.-Y., Chen, S.-P., 2022b. CQDs/ZnO composites based on waste rice noodles: preparation and photocatalytic capability. *RSC Adv.* 12, 23692–23703. <https://doi.org/10.1039/D2RA03709B>.
- Li, L.-H., Li, Y.-L., Hong, Y., 2023. New insights into the microalgal culture using kitchen waste: enzyme pretreatment and mixed microalgae self-flocculation. *Biochem. Eng. J.* 195. <https://doi.org/10.1016/j.bej.2023.108904>.
- Mandal, S.K., Paul, S., Datta, S., Jana, D., 2021. Nitrogenated CQD decorated ZnO nanorods towards rapid photodegradation of rhodamine B: a combined experimental and theoretical approach. *Appl. Surf. Sci.* 563. <https://doi.org/10.1016/j.apsusc.2021.150315>.
- Marugán, J., van Grieken, R., Cassano, A.E., Alfano, O.M., 2007. Quantum efficiency of cyanide photooxidation with TiO<sub>2</sub>/SiO<sub>2</sub> catalysts: multivariate analysis by experimental design. *Catal. Today* 129, 143–151. <https://doi.org/10.1016/j.cattod.2007.06.060>.
- Misra, A.J., Basu, A., Behera, S.K., Mishra, A., Lundborg, C.S., Tripathy, S.K., 2022. Point-of-use photocatalytic device for water disinfection under visible light using ZnO/Gypsum@alginate beads. *J. Environ. Chem. Eng.* 10. <https://doi.org/10.1016/j.jece.2022.107520>.
- Mo, W.Y., Choi, W.M., Man, K.Y., Wong, M.H., 2020. Food waste-based pellets for feeding grass carp (*Ctenopharyngodon idellus*): adding baker's yeast and enzymes to enhance growth and immunity. *Sci. Total Environ.* 707. <https://doi.org/10.1016/j.scitotenv.2019.134954>.
- Modrojan, C., Căprărescu, S., Dăncilă, A.M., Orbuț, O.D., Vasile, E., Purcar, V., 2020. Mixed oxide layered double hydroxide materials: synthesis, characterization and efficient application for Mn<sup>2+</sup> removal from synthetic wastewater. *Materials* 13, 4089. <https://doi.org/10.3390/ma13184089>.
- Modrojan, C., Căprărescu, S., Dăncilă, A.M., Orbuț, O.D., Grumezescu, A.M., Purcar, V., Radișoiu, V., Fierascu, R.C., 2021. Modified composite based on magnetite and polyvinyl alcohol: synthesis, characterization, and degradation studies of the methyl orange dye from synthetic wastewater. *Polymers* 13, 3911. <https://doi.org/10.3390/polym13223911>.
- Murali, G., Modigunta, J.K.R., Park, S., Lee, S., Lee, H., Yeon, J., Kim, H., Park, Y.H., Park, S.Y., Durrant, J.R., Cha, H., An, T.K., In, I., 2021. Enhancing light absorption and prolonging charge separation in carbon quantum dots via Cl-doping for visible-light-driven photocharge-transfer reactions. *ACS Appl. Mater. Interfaces* 13, 34648–34657. <https://doi.org/10.1021/acsmi.1c01879>.
- Nicolaescu, M., Bandas, C., Orha, C., Șerban, V., Lazău, C., Căprărescu, S., 2021. Fabrication of a UV photodetector based on n-TiO<sub>2</sub>/p-CuMnO<sub>2</sub> heterostructures. *Coatings* 11, 1380. <https://doi.org/10.3390/coatings11111380>.
- Pan, J., Zhao, C., Wang, B., Dong, Z., Jiang, Z., Wang, J., Song, C., Zheng, Y., Li, C., 2020. The transparent device of CdS quantum dots modified Cu<sub>2</sub>O/ZnO orderly nano array p-n junction towards the enhanced photovoltaic conversion. *J. Alloy. Compd.* 827. <https://doi.org/10.1016/j.jallcom.2020.154267>.
- Purcar, V., Șomoghi, R., Nițu, S., Nicolae, C.-A., Alexandrescu, E., Gîfu, I., Gabor, A., Stroescu, H., Ianchiș, R., Căprărescu, S., Cintează, L., 2017. The effect of different coupling agents on nano-ZnO materials obtained via the sol-gel process. *Nanomaterials* 7, 439. <https://doi.org/10.3390/nano7120439>.
- Que, Q., Xing, Y., He, Z., Yang, Y., Yin, X., Que, W., 2017. Bi<sub>2</sub>O<sub>3</sub>/Carbon quantum dots heterostructured photocatalysts with enhanced photocatalytic activity. *Mater. Lett.* 209, 220–223. <https://doi.org/10.1016/j.matlet.2017.07.115>.
- Rojas, L.F., Zapata, P., Ruiz-Tirado, L., 2022. Agro-industrial waste enzymes: perspectives in circular economy. *Curr. Opin. Green Sustainable Chem.* 34. <https://doi.org/10.1016/j.cogsc.2021.100585>.
- Samadi, M., Zirak, M., Naseri, A., Khorashadizade, E., Moshfegh, A.Z., 2016. Recent progress on doped ZnO nanostructures for visible-light photocatalysis. *Thin Solid Films* 605, 2–19. <https://doi.org/10.1016/j.tsf.2015.12.064>.
- Sarkar, B., Daware, A.V., Gupta, P., Krishnani, K.K., Baruah, S., Bhattacharjee, S., 2017. Nanoscale wide-band semiconductors for photocatalytic remediation of aquatic pollution. *Environ. Sci. Pollut. Res.* 24, 25775–25797. <https://doi.org/10.1007/s11356-017-0252-3>.
- Senasu, T., Chankhanittha, T., Hemavibool, K., Nanan, S., 2021. Visible-light-responsive photocatalyst based on ZnO/CdS nanocomposite for photodegradation of reactive red azo dye and ofloxacin antibiotic. *Mater. Sci. Semicond. Process.* 123. <https://doi.org/10.1016/j.mssp.2020.105558>.
- Sharma, P., Kumar, N., Chauhan, R., Singh, V., Srivastava, V.C., Bhatnagar, R., 2020. Growth of hierarchical ZnO nano flower on large functionalized rGO sheet for superior photocatalytic mineralization of antibiotic. *Chem. Eng. J.* 392. <https://doi.org/10.1016/j.cej.2019.123746>.
- Shehzad, A., Bashir, M.J.K., Sethupathi, S., Lim, J.-W., 2015. An overview of heavily polluted landfill leachate treatment using food waste as an alternative and renewable source of activated carbon. *Process Saf. Environ. Prot.* 98, 309–318. <https://doi.org/10.1016/j.psep.2015.09.005>.
- Shen, J.-H., Chiang, T.-H., Tsai, C.-K., Jiang, Z.-W., Horng, J.-J., 2022. Mechanistic insights into hydroxyl radical formation of Cu-doped ZnO/g-C<sub>3</sub>N<sub>4</sub> composite

- photocatalysis for enhanced degradation of ciprofloxacin under visible light: Efficiency, kinetics, products identification and toxicity evaluation. *J. Environ. Chem. Eng.* 10, <https://doi.org/10.1016/j.jece.2022.107352> 107352.
- Sugita, T., Kobayashi, K., Yamazaki, T., Isaka, M., Itabashi, H., Mori, M., 2020. Development of evaluation method for photocatalytic ability by ion chromatography combined with a flow-type reactor: application to immobilized photocatalyst materials prepared by double-layer coating method. *J. Photochem. Photobiol. A Chem.* 400, <https://doi.org/10.1016/j.jphotochem.2020.112662> 112662.
- Tan, A., Yang, G., Wan, X., 2021. Ultra-high quantum yield nitrogen-doped carbon quantum dots and their versatile application in fluorescence sensing, bioimaging and anti-counterfeiting. *Spectrochim. Acta A Mol. Biomol. Spectrosc.* 253, <https://doi.org/10.1016/j.saa.2021.119583> 119583.
- Tang, C., Liu, C., Han, Y., Guo, Q., Ouyang, W., Feng, H., Wang, M., Xu, F., 2019. Nontoxic carbon quantum dots/g-C<sub>3</sub>N<sub>4</sub> for efficient photocatalytic inactivation of *Staphylococcus aureus* under visible light. *Adv. Healthc. Mater.* 8, 1801534. <https://doi.org/10.1002/adhm.201801534>.
- Touze-Foltz, N., Xie, H., Stoltz, G., 2021. Performance issues of barrier systems for landfills: a review. *Geotext. Geomembr.* 49, 475–488. <https://doi.org/10.1016/j.geotextmem.2020.10.016>.
- Wang, Z., Guo, Z., Huo, W., He, T., Cao, T., Liu, X., Zhang, Y., Ye, G., Zhang, S., 2020. Facile constructing ZnO/ZnCO<sub>3</sub> heterojunction for high-performance photocatalytic NO oxidation and reaction pathway study. *J. Mater. Sci. Mater. Electron.* 31, 4527–4534. <https://doi.org/10.1007/s10854-020-03002-9>.
- Wang, Z., Xiang, M., Huo, B., Wang, J., Yang, L., Ma, W., Qi, J., Wang, Y., Zhu, Z., Meng, F., 2023. A novel ZnO/CQDs/PVDF piezoelectric system for efficiently degradation of antibiotics by using water flow energy in pipeline: performance and mechanism. *Nano Energy* 107, <https://doi.org/10.1016/j.nanoen.2022.108162> 108162.
- Wu, Y., Liu, Y., Yin, J., Li, H., Huang, J., 2019. Facile ultrasonic synthesized NH<sub>2</sub>-carbon quantum dots for ultrasensitive Co<sup>2+</sup> ion detection and cell imaging. *Talanta* 205, <https://doi.org/10.1016/j.talanta.2019.120121> 120121.
- Xia, Y., Gang, R., Xu, L., Huang, S., Zhou, L., Wang, J., 2020. Nanorod-pillared mesoporous rGO/ZnO/Au hybrids for photocatalytic Cr (VI) reduction: enhanced Cr(VI) adsorption and solar energy harvest. *Ceram. Int.* 46, 1487–1493. <https://doi.org/10.1016/j.ceramint.2019.09.115>.
- Xiao, B., Qin, Y., Zhang, W., Wu, J., Qiang, H., Liu, J., Li, Y.-Y., 2018. Temperature-phased anaerobic digestion of food waste: a comparison with single-stage digestions based on performance and energy balance. *Bioresour. Technol.* 249, 826–834. <https://doi.org/10.1016/j.biortech.2017.10.084>.
- Xie, T., Zhang, Z., Zhang, D., Wei, C., Lin, Y., Feng, R., Nan, J., Feng, Y., 2023. Effect of hydrothermal pretreatment and compound microbial agents on compost maturity and gaseous emissions during aerobic composting of kitchen waste. *Sci. Total Environ.* 854, <https://doi.org/10.1016/j.scitotenv.2022.158712> 158712.
- Xu, Y., Fan, Y., Zhang, L., Wang, Q., Fu, H., She, Y., 2019. A novel enhanced fluorescence method based on multifunctional carbon dots for specific detection of Hg<sup>2+</sup> in complex samples. *Spectrochim. Acta A Mol. Biomol. Spectrosc.* 220, <https://doi.org/10.1016/j.saa.2019.05.014> 117109.
- Xu, H., Xu, L., Ahmed, A., 2023. Carbon quantum dots-decorated ZnO heterostructure nanoflowers grown on nanofiber membranes as high-efficiency photocatalysts. *Diam. Relat. Mater.* 136, <https://doi.org/10.1016/j.diamond.2023.109972> 109972.
- Xue, Y., Xie, Y., Xu, C., He, H., Jiang, Q., Ying, G., Huang, H., 2022. 0D/2D heterojunction of graphene quantum dots/MXene nanosheets for boosted hydrogen evolution reaction. *Surf. Interfaces* 30, <https://doi.org/10.1016/j.surfin.2022.101907> 101907.
- Yan, W., Vadivelu, V., Maspolim, Y., Zhou, Y., 2021. In-situ alkaline enhanced two-stage anaerobic digestion system for waste cooking oil and sewage sludge co-digestion. *Waste Manag.* 120, 221–229. <https://doi.org/10.1016/j.wasman.2020.11.047>.
- Yu, J., Wang, X., Chen, L., Lu, G., Shi, G., Xie, X., Wang, Y., Sun, J., 2022. Enhanced adsorption and visible-light photocatalytic degradation of toluene by CQDs/UiO-66 MOG with hierarchical pores. *Chem. Eng. J.* 435, <https://doi.org/10.1016/j.cej.2022.135033> 135033.
- Zeilekew, O.A., Fufa, P.A., Sabir, F.K., Duma, A.D., 2021. Water hyacinth plant extract mediated green synthesis of Cr<sub>2</sub>O<sub>3</sub>/ZnO composite photocatalyst for the degradation of organic dye. *Heliyon* 7, e07652.
- Zhang, J., Gao, S., Wang, G., Ma, X., Jiao, S., Sang, D., Liu, S., Mao, M., Fang, H., Wang, J., 2019. Tunable Fabrication of CuO Nanoplates on ZnO Nanorods: heterostructure Formation by Photodeposition for Enhanced Photocatalytic Activity. *Eur. J. Inorg. Chem.* 2019, 2654–2660. <https://doi.org/10.1002/ejic.201900401>.
- Zhang, J., Li, L., Du, M., Cui, Y., Li, Y., Yan, W., Huang, H., Li, X., Zhu, X., 2023a. Single-Atom phosphorus defects decorated CoP cocatalyst boosts photocatalytic hydrogen generation performance of Cd 0.5 Zn 0.5 S by directed separating the photogenerated carriers. *Small* 19, <https://doi.org/10.1002/smll.202300402> 2300402.
- Zhang, Y., Ma, H., Chen, X., Wang, W., Li, F., Qiang, T., Shen, Y., Cong, Y., 2023b. CQDs improved the photoelectrocatalytic performance of plasma assembled WO<sub>3</sub>/TiO<sub>2</sub>-NRs for bisphenol A degradation. *J. Hazard. Mater.* 443, <https://doi.org/10.1016/j.jhazmat.2022.130250> 130250.
- Zhang, R., Zhang, A., Yang, Y., Cao, Y., Dong, F., Zhou, Y., 2020. Surface modification to control the secondary pollution of photocatalytic nitric oxide removal over monolithic protonated g-C<sub>3</sub>N<sub>4</sub>/graphene oxide aerogel. *J. Hazard. Mater.* 397, <https://doi.org/10.1016/j.jhazmat.2020.122822> 122822.
- Zhao, Y., Li, Z., Wei, J., Li, X., Shi, H., Cao, B., Fan, J., 2022. Efficient photodegradation of cefixime catalyzed by a direct Z-scheme CQDs-BiOBr/CN composite: performance, toxicity evaluation and photocatalytic mechanism. *Chemosphere* 292, <https://doi.org/10.1016/j.chemosphere.2021.133430> 133430.
- Zhou, G., Long, L., Wang, P., Hu, Y., Zhang, Q., Liu, C., 2020. Designing CuO/ZnO nanoforest device toward optimal photocatalytic performance through structure and facet engineering. *Mater. Lett.* 273, <https://doi.org/10.1016/j.matlet.2020.127907> 127907.
- Zhou, T., Shi, J., Li, G., Liu, B., Hu, B., Che, G., Liu, C., Wang, L., Yan, L., 2023. Advancing n-π\* electron transition of carbon nitride via distorted structure and nitrogen heterocycle for efficient photodegradation: performance, mechanism and toxicity insight. *J. Colloid Interface Sci.* 632, 285–298. <https://doi.org/10.1016/j.jcis.2022.11.073>.